REPORT DOCUMENTATION PAGE

Form Approved
OMB NO. 0704-0188

1. AGENCY USE ONLY (Leave Blank)	2. REPORT DATE 4/20/04	3. REPORT TYPE AND DATES COVERED Reprints

4. TITLE AND SUBTITLE
"Quasi-wavelet calculations of sound scattering behind barriers", Applied Acoustics, V. 65, pp. 605-627 (2004).

5. FUNDING NUMBERS
DAAD19-01-1-0640

6. AUTHOR(S)
D. K. Wilson, V. E. Ostashev, G. H. Goedecke, and H. J. Auvermann

7. PERFORMING ORGANIZATION NAME(S) AND ADDRESS(ES)
Physics Department, New Mexico State University,
Box 30001, Dept. 3D, Las Cruces, NM 88003

8. PERFORMING ORGANIZATION REPORT NUMBER

9. SPONSORING / MONITORING AGENCY NAME(S) AND ADDRESS(ES)
U. S. Army Research Office
P.O. Box 12211
Research Triangle Park, NC 27709-2211

10. SPONSORING / MONITORING AGENCY REPORT NUMBER
42469-EV-H
.15

11. SUPPLEMENTARY NOTES
The views, opinions and/or findings contained in this report are those of the author(s) and should not be construed as an official Department of the Army position, policy or decision, unless so designated by other documentation.

12 a. DISTRIBUTION / AVAILABILITY STATEMENT
Approved for public release; distribution unlimited.

12 b. DISTRIBUTION CODE

13. ABSTRACT (Maximum 200 words)
See the reprint attached.

14. SUBJECT TERMS

15. NUMBER OF PAGES
23

16. PRICE CODE

17. SECURITY CLASSIFICATION OR REPORT	18. SECURITY CLASSIFICATION ON THIS PAGE	19. SECURITY CLASSIFICATION OF ABSTRACT	20. LIMITATION OF ABSTRACT
UNCLASSIFIED	**UNCLASSIFIED**	**UNCLASSIFIED**	**UL**

Available online at www.sciencedirect.com
SCIENCE DIRECT®
Applied Acoustics 65 (2004) 605–627
applied acoustics
www.elsevier.com/locate/apacoust

Quasi-wavelet calculations of sound scattering behind barriers

D. Keith Wilson [a,*], Vladimir E. Ostashev [b,c], George H. Goedecke [c], Harry J. Auvermann [d]

[a] *US Army Cold Regions Research and Engineering Laboratory, 72 Lyme Rd., Hanover, NH 03755, USA*
[b] *NOAA/Environmental Technology Laboratory, 325 Broadway, Boulder, CO 80305, USA*
[c] *Department of Physics, New Mexico State University, Las Cruces, NM 88003, USA*
[d] *6056 N. Jim Miller Rd., Dallas, TX 75228, USA*

Received 30 June 2003; received in revised form 17 November 2003; accepted 28 November 2003

Abstract

Quasi-wavelets (QWs) are a representation of turbulence consisting of self-similar, eddy-like structures with random orientations and positions in space. They are used in this paper to calculate the scattering, due to turbulent velocity fluctuations, of sound behind noise barriers as a function of the size and spatial location of the eddies. The sound scattering cross-section for QWs of an individual size class (eddy size) is derived and shown to reproduce results for the von Kármán spectrum when the scattered energies from a continuous distribution of QW sizes are combined. A Bragg resonance condition is derived for the eddy size that scatters most strongly for a given acoustic wavenumber and scattering angle. Results for scattering over barriers show that, for typical barrier conditions, most of the scattered energy originates from eddies in the size range of approximately one-half to twice the size of the eddies responsible for maximum scattering. The results also suggest that scattering over the barrier due to eddies with a line of sight to both the source and receiver is generally significant only for frequencies above several kilohertz, for sources and receivers no more than a few meters below the top of the barrier, and for very turbulent atmospheric conditions.

PACS: 43.28.Gq; 43.50.Gf; 43.50.Vt

Keywords: Outdoor sound propagation; Noise barriers; Turbulence

* Corresponding author. Tel.: +1-804-828-7520; fax: +1-804-828-5717.
E-mail address: d.keith.wilson@erdc.usace.army.mil (D. Keith Wilson).

0003-682X/$ - see front matter © 2003 Elsevier Ltd. All rights reserved.
doi:10.1016/j.apacoust.2003.11.009

1. Introduction

Turbulence can reduce the effectiveness of outdoor noise barriers by scattering sound energy deep within the diffractive shadow region (that is, the indirectly insonified region) formed by the barrier. Accurate modeling of this phenomenon is quite challenging, as realistic representations for the turbulence in the vicinity of the barrier are required in addition to techniques for calculating the complex sound propagation effects. Daigle [1] provided the first detailed calculations of the scattered and diffracted sound energy behind a barrier, and compared the results to experiments involving detailed acoustical and turbulence measurements. He demonstrated that scattering can significantly impact barrier performance, particularly for frequencies above a few kilohertz.

Recently, a new tool for representing turbulence, called *quasi-wavelets* (QWs) [2,3], was introduced. Unlike Fourier spectral representations of turbulence, QWs have the advantage of being localized in space. This feature makes scattering calculations more straightforward and allows the scattering process to be characterized simultaneously in space and scale of the scatterers. Another improvement is that the QW representation includes scattering from the energy-containing subrange of the turbulence (the large eddies). Goedecke et al. [4] successfully used a QW formulation to calculate the spectral broadening of sound scattered by moving eddies. In this paper, we reexamine the phenomenon of sound scattering over barriers using a QW representation of the turbulence.

The individual QWs are intended to have properties reminiscient of actual eddies in a turbulent flow. The general technique of representing turbulence in wave scattering calculations as a collection of discrete, eddy-like structures (sometimes called *turbules*) apparently originates with DeWolfe [5]. More recently, McBride et al. [6] used such a representation for scattering of sound above a complex impedance boundary, and Boulanger et al. [7] used it to determine turbulence effects on sonic booms. We call the eddy-like structures quasi-wavelets when the ensemble is constructed from a parent function in a systematic, self-similar manner.

The paper is organized as follows. We provide an overview of the QW model formulation, together with some new results for determination of the model parameters, in Section 2. Equations are derived in Section 3 for the scattered field from a single QW and for the scattering cross-section of a random spatial distribution of QWs belonging to a single size class (eddy size). When the scattered energies from a continuous distribution of QW size classes are combined, the resulting cross-section agrees with a previous result for the von Kármán turbulence spectrum. In Section 4, QWs are applied to the problem of sound scattering over a barrier. The results illustrate the eddy scales primarily responsible for scattering as well as the spatial regions from which the scattered energy originates.

2. Quasi-wavelet ensembles

Turbulence is generally conceived as a collection of eddies of many different sizes [8,9]. The QW model is a mathematical representation of turbulence that more

closely resembles this physical picture than Fourier modes or customary wavelets. Like customary wavelets [10,11], the QW representation is based on self-similar application of a spatially localized parent function. In contrast to customary wavelets, however, the orientations and positions of the quasi-wavelets are random. Furthermore, the QW basis functions are not required to be mutually orthogonal or to form a mathematically complete set.

Recently, a QW representation has been developed that reproduces the von Kármán turbulent velocity spectrum [3], which generally fits atmospheric turbulence well. In [2], expressions for temperature and velocity fluctuation spectra for isotropic homogeneous turbulence were obtained using QW (turbule) superpositions. Only the velocity spectra are considered in this paper. The relationship between the QW parent function and the turbulence kinetic energy spectrum is discussed in this section in detail. The parameters of the QW ensemble are related to the inertial-subrange characteristics of the turbulence.

2.1. General results

Like customary wavelets, QWs are derived from translations and dilatations of a dimensionless, spatially localized parent function $f(\xi)$. Here, ξ is the magnitude of the vector $\boldsymbol{\xi} \equiv (\mathbf{r} - \mathbf{b}^{\alpha n})/a_\alpha$, where $\mathbf{r}$ is the spatial coordinate, $\mathbf{b}^{\alpha n}$ is the center of the QW, and a_α is its size. The index α indicates the size class of the QW, with $\alpha = 1$ being the largest size and $\alpha = N$ the smallest, and n indicates a particular QW within that size class. The size a_1 is associated with the outer scale of the turbulence and a_N with the inner scale. By defining the velocity field $\mathbf{v}^{\alpha n}(\mathbf{r})$ as the curl of a vector potential $\mathbf{A}^{\alpha n}(\mathbf{r})$, we assure that the turbulence will be a solenoidal field. Hence, we set $\mathbf{v}^{\alpha n}(\mathbf{r}) = \nabla \times \mathbf{A}^{\alpha n}(\mathbf{r})$, where

$$\mathbf{A}^{\alpha n}(\mathbf{r}) = \boldsymbol{\Omega}^{\alpha n} a_\alpha^2 f(\xi) \tag{1}$$

and $\boldsymbol{\Omega}^{\alpha n}$ is the angular velocity vector of the QW. The presence of a_α^2 in the definition provides dimensional consistency. Writing out the curl of the potential leads to the following result for the rotational velocity field associated with the QW:

$$\mathbf{v}^{\alpha n}(\mathbf{r}) = \boldsymbol{\Omega}^{\alpha n} \times (\mathbf{r} - \mathbf{b}^{\alpha n})\left(-\xi^{-1}\partial f/\partial \xi\right). \tag{2}$$

Since turbulence and scattering processes are often studied in spectral domain, we will have use for the Fourier transform of the velocity field. By definition,

$$\tilde{\mathbf{v}}(\boldsymbol{\kappa}) = \frac{1}{(2\pi)^3} \int \mathrm{d}^3 r \, \mathrm{e}^{-\mathrm{i}\boldsymbol{\kappa}\cdot\mathbf{r}} \mathbf{v}(\mathbf{r}), \tag{3}$$

in which $\boldsymbol{\kappa}$ is the wavenumber vector for the turbulence. Transformation of Eq. (2) leads to

$$\tilde{\mathbf{v}}^{\alpha n}(\boldsymbol{\kappa}) = \mathrm{i}\boldsymbol{\kappa} \times \tilde{\mathbf{A}}^{\alpha n}(\boldsymbol{\kappa}) = \mathrm{i}(\boldsymbol{\kappa} \times \boldsymbol{\Omega}^{\alpha n}) \exp\left(-\mathrm{i}\boldsymbol{\kappa} \cdot \mathbf{b}^{\alpha n}\right) a_\alpha^5 F(\kappa a_a), \tag{4}$$

where

$$F(y) = \frac{1}{(2\pi)^3} \int \mathrm{d}^3\xi \, \mathrm{e}^{-\mathrm{i}\mathbf{y}\cdot\boldsymbol{\xi}} f(\xi) \tag{5}$$

is the spectrally transformed parent function.

A key distinction between QWs and customary wavelets is that the orientation of the QWs, $\hat{\boldsymbol{\Omega}}^{\alpha n}$ (where the carat indicates a unit vector), and their eddy centers, $\mathbf{b}^{\alpha n}$, are random variables. For a homogeneous, isotropic model, the $\hat{\boldsymbol{\Omega}}^{\alpha n}$ are statistically independent and distributed uniformly over all directions, and the $\mathbf{b}^{\alpha n}$ are statistically independent and distributed uniformly in a volume of interest V. This construction is illustrated in Fig. 1. The total velocity field created by the quasi-wavelets (the QW ensemble), found by superposition, is

$$\mathbf{v}(\mathbf{r}) = \sum_{\alpha=1}^{N} \sum_{n=1}^{N_\alpha} \mathbf{v}^{\alpha n}(\mathbf{r}), \tag{6}$$

where N is the number of size classes and N_α is the number of QWs for the size class α. We may define the spectral density tensor $\Phi_{ij}(\boldsymbol{\kappa})$ of the velocity fluctuations as

$$\Phi_{ij}(\boldsymbol{\kappa}) = \frac{(2\pi)^3}{V} \left\langle \tilde{v}_i(\boldsymbol{\kappa}) \tilde{v}_j^*(\boldsymbol{\kappa}) \right\rangle, \tag{7}$$

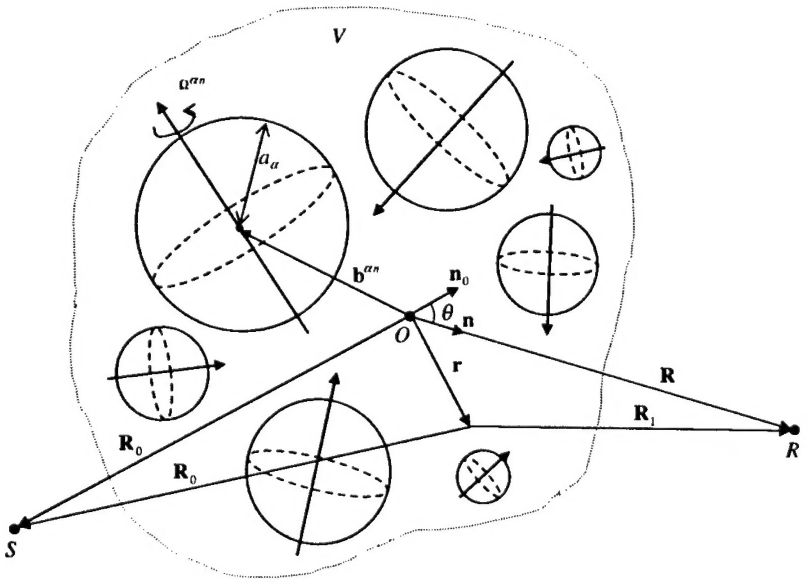

Fig. 1. Distribution of quasi-wavelets in a volume V. Each QW has a random position $\mathbf{b}^{\alpha n}$ and angular velocity vector $\boldsymbol{\Omega}^{\alpha n}$, where α is an index for the size class of the QW and n is an index for the QWs within each size class. The nominal size of the QW is a_α. Also shown is the geometry used for calculating scattering by a QW in Section 3. The source position is indicated as S, the receiver position as R, and the origin as O. The vector $\mathbf{r}$ extends from the origin to the field point at which the scattering is calculated.

where $\langle\rangle$ is the ensemble average (average of a large number of random realizations) over the $\hat{\boldsymbol{\Omega}}$ and $\mathbf{b}$ variables. Substituting with Eq. (4) and recalling that the QWs have statistically independent orientations, we find

$$\Phi_{ij}(\boldsymbol{\kappa}) = \frac{(2\pi)^3}{V}\sum_{\alpha=1}^{N} N_\alpha a_\alpha^{10} F^2(\kappa a_\alpha)\left\langle[(\boldsymbol{\kappa}\times\boldsymbol{\Omega}^{\alpha n})\cdot\mathbf{e}_i]\left[(\boldsymbol{\kappa}\times\boldsymbol{\Omega}^{\alpha n})\cdot\mathbf{e}_j\right]\right\rangle, \tag{8}$$

where $\mathbf{e}_i$ is the unit vector in the ith direction. Since the angular velocity magnitude is the same for all members of a size class, we may define $\Omega_\alpha = |\boldsymbol{\Omega}^{\alpha n}|$. Writing out the components of this equation and noting that the cross-correlations of the angular velocity components (e.g., $\langle\Omega_x^{\alpha n}\Omega_y^{\alpha n}\rangle$) are zero, whereas the autocorrelations (e.g., $\langle(\Omega_x^{\alpha n})^2\rangle$) must equal $\Omega_\alpha^2/3$, we find

$$\Phi_{ij}(\boldsymbol{\kappa}) = \frac{(2\pi)^3}{3V}\left(\kappa^2\delta_{ij} - \kappa_i\kappa_j\right)\sum_{\alpha=1}^{N} N_\alpha \Omega_\alpha^2 a_\alpha^{10} F^2(\kappa a_\alpha), \tag{9}$$

where $\delta_{ij} = 1$ when $i = j$ and 0 otherwise. As is well known in the theory of isotropic turbulence, the spectral tensor can be written as $\Phi_{ij}(\boldsymbol{\kappa}) = E(\kappa)(\kappa^2\delta_{ij} - \kappa_i\kappa_j)/(4\pi\kappa^4)$, where $E(\kappa)$ is the turbulent kinetic energy (per unit mass) spectrum [9]. Using this formula and Eq. (9), we have

$$E(\kappa) = \frac{32\pi^4\kappa^4}{3V}\sum_{\alpha=1}^{N} N_\alpha \Omega_\alpha^2 a_\alpha^{10} F^2(\kappa a_\alpha). \tag{10}$$

The spectral properties of the QW model are dependent upon the choice of $F(y)$ and the scaling of Ω_α and N_α with a_α. Let us construct the representation such that the packing fractions,

$$\varphi_\alpha \equiv N_\alpha a_\alpha^3/V, \tag{11}$$

equal a constant value φ, independent of the eddy size class α. Next, we choose the angular velocity magnitudes according to Kolmogorov's [12] original hypotheses for the inertial subrange. According to that treatment, quantities in the inertial subrange depend only on the eddy size (a_α in our notation) and the dissipation rate of specific turbulent kinetic energy, ϵ. By dimensional analysis (since ϵ has dimensions length^2 time^{-3}), we must have

$$\Omega_\alpha = c_\Omega a_\alpha^{-2/3}\epsilon^{1/3}, \tag{12}$$

where c_Ω is a constant. Substituting these scalings into (10) yields

$$E(\kappa) = \frac{32\pi^4\varphi c_\Omega^2\epsilon^{2/3}\kappa^4}{3}\sum_{\alpha=1}^{N} a_\alpha^{17/3} F^2(\kappa a_\alpha). \tag{13}$$

This result shows that we can adjust the product φc_Ω^2 in order to obtain a desired turbulent kinetic energy.

As with customary wavelets, the QW size classes are chosen to scale in a self-similar fashion; that is, $a_{\alpha+1}/a_\alpha = \text{const}$. For convenience, we define a constant $\mu > 0$ such that

$$a_{\alpha+1}/a_\alpha = \mathrm{e}^{-\mu}. \tag{14}$$

When the size classes are very closely spaced, this relationship implies $\Delta a_\alpha \equiv a_{\alpha+1} - a_\alpha \simeq -\mu a_\alpha$. Therefore,

$$\begin{aligned} E(\kappa) &\simeq -\frac{32\pi^4\varphi c_\Omega^2\epsilon^{2/3}\kappa^4}{3\mu}\sum_{\alpha=1}^{N}\Delta a_\alpha a_\alpha^{14/3}F^2(\kappa a_\alpha) \\ &\simeq \frac{32\pi^4\varphi c_\Omega^2\epsilon^{2/3}\kappa^4}{3\mu}\int_{a_N}^{a_1}\mathrm{d}a\; a^{14/3}F^2(\kappa a). \end{aligned} \tag{15}$$

With the substitution $y = \kappa a$, we have

$$E(\kappa) \simeq \frac{32\pi^4\varphi c_\Omega^2\epsilon^{2/3}\kappa^{-5/3}}{3\mu}\int_{\kappa a_N}^{\kappa a_1}\mathrm{d}y\; y^{14/3}F^2(y). \tag{16}$$

The ratio φ/μ can be removed from this expression by noting that the total number of quasi-wavelets in the representation is

$$N_{\mathrm{QW}} = \sum_{\alpha=1}^{N} N_\alpha = \varphi V\sum_{\alpha=1}^{N} a_\alpha^{-3} \simeq (\varphi V/\mu)\int_{a_N}^{a_1}\mathrm{d}a\; a^{-4}. \tag{17}$$

The integration results in

$$N_{\mathrm{QW}} \simeq \frac{\varphi V}{3\mu}\left(a_N^{-3} - a_1^{-3}\right). \tag{18}$$

Solving for the ratio φ/μ, we may now rewrite Eq. (16) as

$$E(\kappa) \simeq \frac{32\pi^4 N_{\mathrm{QW}} c_\Omega^2\epsilon^{2/3}\kappa^{-5/3}}{V}\left(a_N^{-3} - a_1^{-3}\right)^{-1}\int_{\kappa a_N}^{\kappa a_1}\mathrm{d}y\; y^{14/3}F^2(y). \tag{19}$$

To maintain a fixed value of the energy spectrum $E(\kappa)$, c_Ω^2 must be varied in proportion to the inverse of the number of quasi-wavelets per unit volume.

We next turn to the matter of relating the parameters of the QW ensemble to known properties of the turbulence. The energy spectrum in the inertial subrange has been shown empirically to obey the equation [13,14]

$$E(\kappa) = (55\alpha_v/18)\epsilon^{2/3}\kappa^{-5/3}, \tag{20}$$

where α_v, an empirical constant, has the approximate value 0.52. Comparing Eqs. (19) and (20), we have for wavenumbers κ the inertial subrange ($a_1^{-1} \ll \kappa \ll a_N^{-1}$),

$$\frac{55\alpha_v}{18} = \frac{32\pi^4 N_{\mathrm{QW}} c_\Omega^2}{V}\left(a_N^{-3} - a_1^{-3}\right)^{-1}\int_{\kappa a_N}^{\kappa a_1}\mathrm{d}y\; y^{14/3}F^2(y). \tag{21}$$

The preceding equality can be satisfied by setting

$$c_\Omega^2 = \frac{55\alpha_v V}{576\pi^4 N_{QW}}\left(a_N^{-3} - a_1^{-3}\right) = \frac{55\alpha_v \mu}{192\pi^4 \varphi} \tag{22}$$

and normalizing the function $F(y)$ such that

$$\int_{\kappa a_N}^{\kappa a_1} \mathrm{d}y\, y^{14/3} F^2(y) = 1. \tag{23}$$

Since $\kappa a_1 \gg 1$ and $\kappa a_N \ll 1$ for κ in the inertial subrange (and anticipating that realistic spectral parent functions will be monotonically decreasing in y, well behaved near $y = 0$, and very small for $y \gg 1$), the limits on the integral may be replaced by 0 and ∞, resulting in the following normalization condition:

$$\int_0^\infty \mathrm{d}y\, y^{14/3} F^2(y) = 1. \tag{24}$$

Combining (22) and (19), we have

$$E(\kappa) = \frac{55\alpha_v}{18}\epsilon^{2/3}\kappa^{-5/3}\int_{\kappa a_N}^{\kappa a_1} \mathrm{d}y\, y^{14/3} F^2(y). \tag{25}$$

Eq. (25) provides the energy spectrum from a prescribed $F(y)$. In some applications, we may wish to reverse the process by calculating $F(y)$ from a prescribed energy spectrum. Multiplying both sides of Eq. (25) by $\kappa^{5/3}$, putting $a_N = 0$ (neglecting the effect of dissipation on the energy spectrum), and differentiating with respect to κ yields an equation for $F^2(\kappa a_1)$,

$$F^2(\kappa a_1) = \frac{18}{55\alpha_v}\epsilon^{-2/3} a_1^{-17/3}\kappa^{-14/3}\frac{\mathrm{d}}{\mathrm{d}\kappa}\left[\kappa^{5/3} E(\kappa)\right]. \tag{26}$$

2.2. Von Kármán quasi-wavelet

The von Kármán energy spectrum has been found useful for calculations of sound propagation in the turbulent atmosphere [15,16]. It is given by

$$E_v(\kappa) = \frac{55\Gamma(5/6)}{9\sqrt{\pi}\Gamma(1/3)}\frac{\sigma_v^2 \kappa^4 L_v^5}{\left(1+\kappa^2 L_v^2\right)^{17/6}}, \tag{27}$$

where σ_v^2 is the variance and L_v an outer length scale. Taking the limit $\kappa L_v \to \infty$ and matching the result with Eq. (20) for the inertial subrange yields a relation among L_v, σ_v, and ϵ:

$$L_v = \left[\frac{2\Gamma(5/6)}{\alpha_v\sqrt{\pi}\Gamma(1/3)}\right]^{3/2}\frac{\sigma_v^3}{\epsilon}. \tag{28}$$

A spectral parent function that yields the von Kármán spectrum can be determined from Eq. (26). The result is

$$F_v^2(y) = \frac{17}{3}\left(\frac{L_v}{a_1}\right)^{17/3}\left(1+\frac{L_v^2 y^2}{a_1^2}\right)^{-23/6}. \tag{29}$$

It can be shown, by substituting Eq. (29) into Eq. (24), that the normalization condition is satisfied for any value of the ratio L_v/a_1. Normally, one would take the largest size class to be near the outer scale; that is, $L_v/a_1 \sim 1$.

The spatial parent function $f_v(\xi)$ (the "von Kármán QW") is found by substituting Eq. (29) into the inverse of Eq. (5). Because of the spherical symmetry, the inverse transform reduces to the following integral:

$$f(\xi) = \frac{4\pi}{\xi} \int_0^\infty dy\, y \sin(y\xi) F(y). \tag{30}$$

With $F(y)$ given by Eq. (29), the integral can be found in tables [17]. After some algebra, the result is

$$f_v(\xi) = \frac{17^{1/2} 2^{7/12} \pi^{3/2}}{3^{1/2} \Gamma(23/12)} \left(\frac{a_1}{L_v}\right)^{1/6} \left(\frac{\xi a_1}{L_v}\right)^{5/12} K_{5/12}\left(\frac{\xi a_1}{L_v}\right), \tag{31}$$

where K_ν is the modified Bessel function of the second kind.

Fig. 2 shows QW energy spectra based on Eq. (29) for representations with $N_\alpha = 4$ and $N_\alpha = 64$ size classes. The actual von Kármán energy spectrum (Eqs. (27) and (28)) and the Kolmogorov spectrum (Eq. (20)) are shown for comparison. The length scales for the calculations are such that $a_1 = L_v = 1000 a_N$. We see that the QW

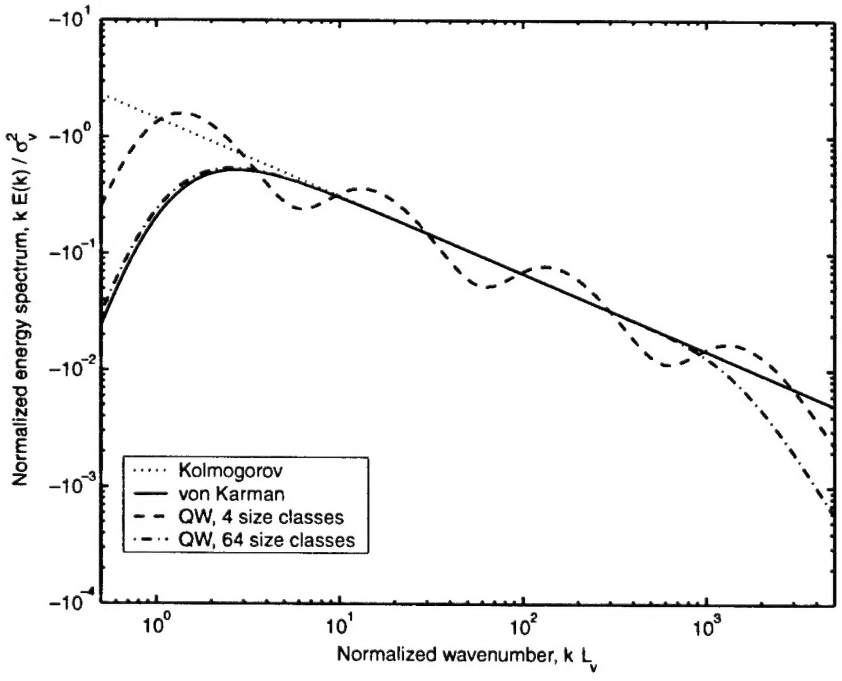

Fig. 2. Energy spectra resulting from QW representations with 4 and 64 discrete size classes. The von Kármán and Kolmogorov energy spectra are shown for comparison.

representation with 64 size classes is essentially the same as the von Kármán spectrum within the energy-containing ($\kappa L_v \lesssim 5$) and inertial ($5 \lesssim \kappa L_v \lesssim 500$) subranges. Within the dissipative subrange ($\kappa L_v \gtrsim 500$), the QW representation exhibits rapid diminishment in the spectrum with increasing wavenumber. This spectral roll-off, which is similar to that found in actual turbulence, is not present in the von Kármán spectrum because Eq. (27) does not model it. The QW representation with four size classes produces a very bumpy spectrum that is not consistently close to the von Kármán spectrum. These results suggest that QW representations with approximately 20 or more size classes per decade provide smooth, accurate spectral models.

3. Scattering by quasi-wavelets

Let us first consider the scattering from a single QW. Fig. 1 defines the scattering geometry. Here, $\mathbf{R}$ is the vector from the origin to the receiver, $\mathbf{R}_0$ is the vector from the origin to the source, $\mathbf{n} = \mathbf{R}/|\mathbf{R}|$, $\mathbf{n}_0 = -\mathbf{R}_0/|\mathbf{R}_0|$, $\mathbf{k} = k\mathbf{n}$, $\mathbf{k}_0 = k\mathbf{n}_0$, and θ is the angle between $\mathbf{n}$ and $\mathbf{n}_0$. The acoustic wavenumber k is $2\pi f/c_0$, where f is frequency and c_0 is the background sound speed. The pressure field associated with the wave propagating spherically from the source is $p_0(\mathbf{R} - \mathbf{R}_0) = A\exp(\mathrm{i}k|\mathbf{R} - \mathbf{R}_0|)/|\mathbf{R} - \mathbf{R}_0|$, where A is the pressure amplitude 1 m from the source. For single scattering by velocity fluctuations, the scattered pressure field is [18, Eq. (7.6)]

$$p_S(\mathbf{R}) = -\frac{Ak^2}{4\pi RR_0}\int_V \mathrm{d}^3 r \exp\left[\mathrm{i}k\left(R_0' + R_1'\right)\right]\left[\frac{2\cos\theta\ \mathbf{n}_0\cdot\mathbf{v}(\mathbf{r})}{c_0}\right]. \tag{32}$$

The primed vectors $\mathbf{R}_0'$ and $\mathbf{R}_1'$ extend from a point in the scattering volume to the source and receiver, respectively. With the approximations $kR_1' \simeq kR - \mathbf{r}\cdot\mathbf{k}$ and $kR_0' \simeq kR_0 + \mathbf{r}\cdot\mathbf{k}_0$ (valid for $R, R_0 \gg V^{1/3}, kL_0V^{1/3}$, where L_0 is the outer length scale of turbulence, as discussed in section 7.1.2 of [18]), we may interpret the integral in the previous expression as a Fourier transform. Applying Eq. (3), we thus have

$$p_S(\mathbf{R}) = -\frac{2\pi^2 Ak^2}{RR_0}\exp\left[\mathrm{i}k(R + R_0)\right]\left[\frac{2\cos\theta\ \mathbf{n}_0\cdot\tilde{\mathbf{v}}(-\mathbf{K})}{c_0}\right], \tag{33}$$

where $\mathbf{K} = \mathbf{k}_0 - \mathbf{k} = k(\mathbf{n}_0 - \mathbf{n})$ is the scattering vector. For a single, rotating QW, substitution with Eq. (4) gives a formula for the single-scattered sound field

$$p_S^{\alpha n}(\mathbf{R}) = \frac{\mathrm{i}4\pi^2 Ak^2 a_\alpha^5 F(Ka_\alpha)\cos\theta}{c_0 RR_0}\exp\left[\mathrm{i}k(R + R_0 - (\mathbf{n} - \mathbf{n}_0)\cdot\mathbf{b}^{\alpha n})\right][\mathbf{n}_0\cdot(\mathbf{K}\times\boldsymbol{\Omega}^{\alpha n})]. \tag{34}$$

The ranges of applicability of the single scattering approximation are given by Eqs. (7.13) and (7.14) in [18].

The total scattered field is a sum of $p_S^{\alpha n}(\mathbf{R})$ over α and n; that is, the sum of the fields scattered by all QWs. To calculate the mean intensity of the total scattered field, one needs to multiply the total field by its complex conjugate and then average

over random positions $\mathbf{b}^{\alpha n}$ and angular velocities $\mathbf{\Omega}^{\alpha n}$. Since the $\mathbf{b}^{\alpha n}$ are statistically independent and randomly distributed, the contribution to the intensity will be zero for the cross-terms involving two distinct QWs (different value of α or n). Therefore, the intensity of the total scattered field is the incoherent sum of intensities of the sound fields scattered by the individual QWs.

Let us now determine the mean-square sound pressure $\langle|p_S^{\alpha n}|^2\rangle$ for an individual QW with $\mathbf{\Omega}^{\alpha n}$ varying randomly in orientation. This requires an evaluation of $\langle[\mathbf{n}_0 \cdot (\mathbf{K} \times \mathbf{\Omega}^{\alpha n})]^2\rangle$. Writing out the components of this equation and applying the properties of the angular velocity correlations that were described in Section 2.1, we find

$$\left\langle [\mathbf{n}_0 \cdot (\mathbf{K} \times \mathbf{\Omega}^{\alpha n})]^2 \right\rangle = \frac{k^2 \Omega_\alpha^2}{3} |\mathbf{n}_0 \times \mathbf{n}|^2. \tag{35}$$

Since $|\mathbf{n}_0 \times \mathbf{n}|^2 = \sin^2\theta$ and $K = k\sqrt{2(1 - \mathbf{n} \cdot \mathbf{n}_0)} = k\sqrt{2(1 - \cos\theta)} = 2k\sin(\theta/2)$, we thus have for the mean-square pressure field scattered by a single QW,

$$\left\langle |p_S^{\alpha n}|^2 \right\rangle = \frac{16\pi^4 A^2 k^6 \Omega_\alpha^2 a_\alpha^{10} F^2(2ka_\alpha \sin\theta/2) \sin^2\theta \cos^2\theta}{3c_0^2 R^2 R_0^2}. \tag{36}$$

For the von Kármán spectral function, Eq. (29), this becomes

$$\left\langle |p_S^{\alpha n}|^2 \right\rangle = \frac{272\pi^4 A^2 k^6 \Omega_\alpha^2 a_\alpha^{10} \sin^2\theta \cos^2\theta}{9c_0^2 R^2 R_0^2} \left(\frac{L_v}{a_1}\right)^{17/3} \times \left(1 + \frac{4k^2 L_v^2 a_\alpha^2 \sin^2(\theta/2)}{a_1^2}\right)^{-23/6}. \tag{37}$$

To find the scattered mean-square pressure $|p_S^\alpha|^2$ from all QWs of a given class size within some scattering volume V, the contributions from each QW are simply added incoherently, as described earlier: $\langle|p_S^\alpha|^2\rangle = \sum_{n=1}^{N_\alpha} \langle|p_S^{\alpha n}|^2\rangle = N_\alpha \langle|p_S^{\alpha n}|^2\rangle$. Making substitutions with Eqs. (11), (12) and (22), we therefore have

$$\left\langle |p_S^\alpha|^2 \right\rangle = \frac{935\alpha_v \mu A^2 k^6 \epsilon^{2/3} V a_\alpha^{17/3} \sin^2\theta \cos^2\theta}{108c_0^2 R^2 R_0^2} \left(\frac{L_v}{a_1}\right)^{17/3} \times \left(1 + \frac{4k^2 L_v^2 a_\alpha^2 \sin^2(\theta/2)}{a_1^2}\right)^{-23/6}. \tag{38}$$

This result provides a decomposition of the scattering based on the size of the turbulent eddies. It applies to scattering from both the energy-containing and inertial subranges of the turbulence. In the following section of this paper, we will use Eq. (38) to determine the location and size of the eddies primarily responsible for scattering of sound energy over barriers.

The scattering cross-section per unit volume into a unit solid angle is defined as (e.g., [18], p. 188)

$$\sigma(\theta) = \frac{\langle I_S \rangle R^2}{I_0 V}, \tag{39}$$

where $\langle I_S \rangle = \langle |p_S|^2 \rangle / (2\rho_0 c_0)$ is the scattered intensity and $I_0 = A^2/(2\rho_0 c_0 R_0^2)$ is the unscattered intensity incident on the volume. Eq. (38) leads to the following scattering cross-section for each size class:

$$\sigma^\alpha(\theta) = \frac{935\alpha_v \mu k^6 \epsilon^{2/3} a_\alpha^{17/3} \sin^2\theta \cos^2\theta}{108 c_0^2} \left(\frac{L_v}{a_1}\right)^{17/3} \left(1 + \frac{4k^2 L_v^2 a_\alpha^2 \sin^2(\theta/2)}{a_1^2}\right)^{-23/6}. \tag{40}$$

Consider the ratio of the cross-section for scatterers of size class α to size class 1. Using the previous equation, we can write this as

$$\frac{\sigma^\alpha(\theta)}{\sigma^1(\theta)} = \left(\frac{a_\alpha}{a_1}\right)^{17/3} \left[\frac{1+q^2}{1+(qa_\alpha/a_1)^2}\right]^{23/6}, \tag{41}$$

where $q \equiv 2kL_v \sin(\theta/2) = kL_v$ is a normalized scattering vector. Fig. 3 shows this ratio as a function of q for various values of a_1/a_α. Note that relatively large eddies scatter most efficiently for small q (forward scattering and/or wavelengths small compared to L_v), whereas relatively small eddies scatter most efficiently for large q (large-angle scattering and/or wavelengths small compared to L_v), as previously

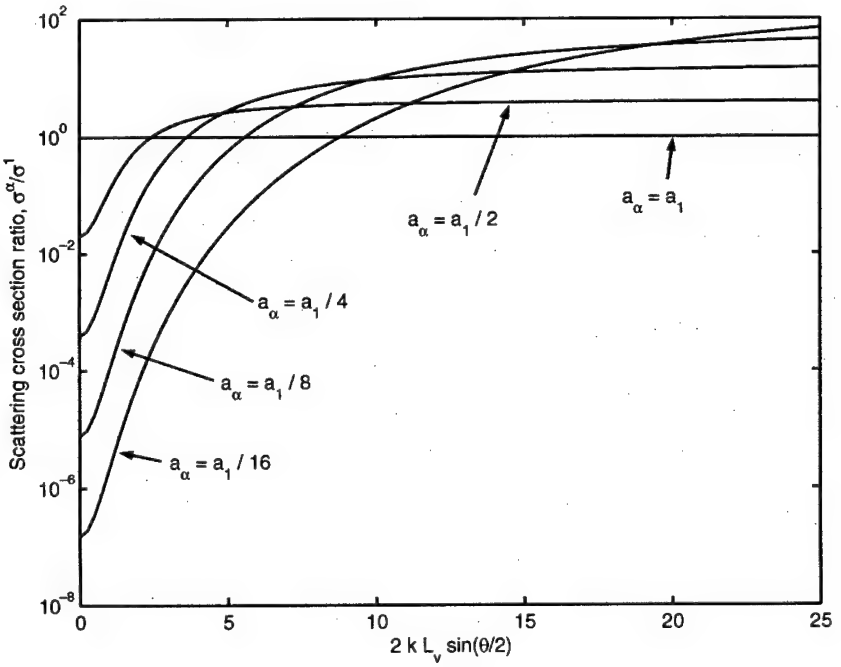

Fig. 3. Ratio of the scattering cross-section σ^α for QWs in the size class α to σ^1 for QWs in the largest size class. Results for various values of a_1/a_α are shown as a function of $2kL_v \sin(\theta/2)$, where L_v is the von Kármán outer length scale and θ the scattering angle.

emphasized in [4]. By differentiating the preceding expression with respect to the ratio a_α/a_1, one finds that QWs with the size $a_\alpha/a_1 = \sqrt{17/6}/q$ are the strongest scatterers. Alternatively, we could write this condition as $ka_\alpha \sin(\theta/2) = \sqrt{17/24}(a_1/L_v)$, which casts the result as a Bragg scattering resonance for a given value of the ratio a_1/L_v.

To check Eq. (38), let us compare it now to previous results for scattering from a continuous distribution of eddy sizes. Summing Eq. (38) over the size index α and then taking the continuous limit (as was done in a similar context in Section 2.1), we have

$$\left\langle |p_S|^2 \right\rangle = \frac{935A^2k^{1/3}\alpha_v\epsilon^{2/3}V\sin^2\theta\cos^2\theta}{108c_0^2R^2R_0^2}\left(\frac{L_v}{a_1}\right)^{17/3}\int_{ka_N}^{ka_1} dy\, y^{14/3} \times \left(1+\frac{4y^2L_v^2\sin^2(\theta/2)}{a_1^2}\right)^{-23/6}. \tag{42}$$

As before, we may replace the lower limit on the integration by 0 when k is within the energy-containing or inertial subrange. The integration may then be performed by making the substitution $t = 1 + (2L_v \sin(\theta/2)/a_1)^{-2}y^{-2}$, with result

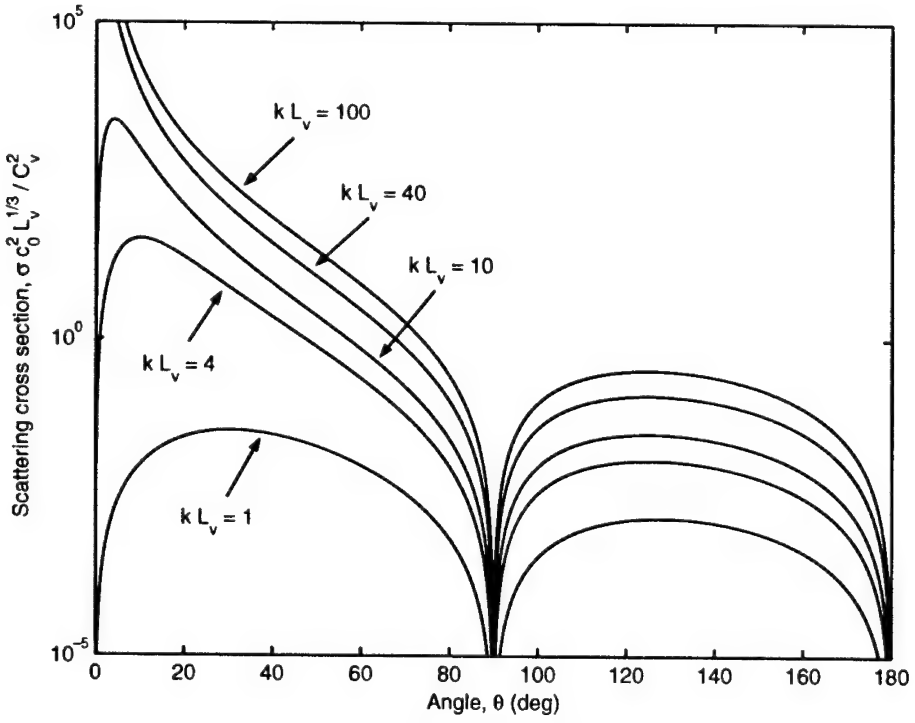

Fig. 4. Total scattering cross-section (normalized by multiplication with $c_0^2L_v^{1/3}/C_v^2$) for the von Kármán turbulence spectrum as a function of scattering angle. Various values of kL_v are shown.

$$\left\langle |p_S|^2 \right\rangle = \frac{55A^2k^{1/3}\alpha_v\epsilon^{2/3}V\sin^2\theta\cos^2\theta}{36c_0^2R^2R_0^2\left[(2\sin(\theta/2))^2 + (kL_v)^{-2}\right]^{17/6}}. \tag{43}$$

Substituting the structure–function parameter $C_v^2 = (3/2)\Gamma(1/3)\alpha_v\epsilon^{2/3}$ [16, Eq.(20)], the overall scattering cross-section becomes

$$\sigma(\theta) = \frac{55k^{1/3}C_v^2\sin^2\theta\cos^2\theta}{54\Gamma(1/3)c_0^2\left[(2\sin(\theta/2))^2 + (kL_v)^{-2}\right]^{17/6}}. \tag{44}$$

This result agrees with [19], which was derived for the von Kármán velocity spectrum. For the inertial subrange, $kL_v \gg 1$, the cross-section reduces to Eq. (7.17) in [18], which was derived from the Kolmogorov spectrum. Fig. 4 shows the dependence of Eq. (44) on θ for various values of kL_v.

4. Application of QWs to scattering over barriers

The geometry of the barrier scattering problem is illustrated by Fig. 5. For simplicity, in this paper the ground is assumed rigid and the reflections are, therefore, represented by an image source and an image receiver. We consider four possible transmission paths involving scattering by turbulence: source–scatterer–receiver (line SOR), source–ground reflection–scatterer–receiver (line WOR), source–scatterer–ground reflection–receiver (line SOU), and source–ground reflection–scatterer–ground reflection–receiver (line WOU).

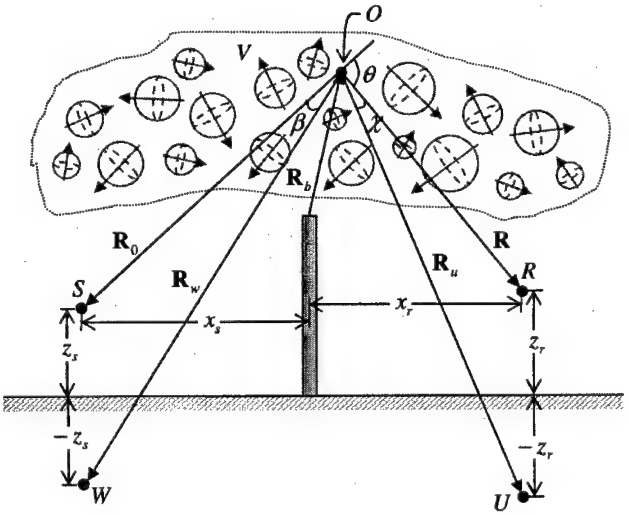

Fig. 5. Geometry for sound scattering over a barrier. A scattering volume V populated with random QWs is shown above the barrier. S is the position of the actual source, W the image source, R the actual receiver, and U the image receiver.

To examine the spatial properties of the scattering process, we partition the total scattering volume V into a number of subvolumes δV_i and calculate the scattering cross-section $\sigma_i^\alpha(\theta_i)$ for each subvolume and QW size class. As a practical matter, each subvolume is treated as an effective point scatterer. This is reasonable when the distances between the subvolume and the source and receiver (R and R_0, respectively) are many wavelengths long. Note that the derivation of the scattering cross-section in the previous section already assumed this condition. Neglecting for a moment the ground reflections, Eqs. (38) and (40) allow us to write the received mean-square scattered pressure attributable to the given scattering subvolume and size class in the following form:

$$\left\langle |p_i^\alpha|^2 \right\rangle = A^2 |G(\mathbf{R}_{0,i} + \mathbf{R}_{b,i}, \mathbf{R}_{b,i})|^2 \delta V_i \sigma^\alpha(\theta_i) |G(\mathbf{R}_{b,i}, \mathbf{R}_i + \mathbf{R}_{b,i})|^2,$$

where $\mathbf{R}_{0,i}$, $\mathbf{R}_i$, and $\mathbf{R}_{b,i}$ are the vectors from the center of the scattering subvolume to the source, receiver, and the top of the barrier, respectively. The angle θ_i is the scattering angle for the subvolume, as defined in Fig. 5. The function $G(\mathbf{R}_s, \mathbf{R}_r)$ is the Green function for propagation from the source at position $\mathbf{R}_s$ to the receiver at position $\mathbf{R}_r$ with the vectors defined relative to the top of the barrier. In free space, we would have simply $G(\mathbf{R}_s, \mathbf{R}_r) = \exp(ik|\mathbf{R}_s - \mathbf{R}_r|)/|\mathbf{R}_s - \mathbf{R}_r|$. However, it is more suitable to use the Green function for the sound field in the vicinity of a barrier that includes diffraction behind the barrier. The calculations in this paper use Pierce's [20] Eq. (9-9.1), for this purpose. (The function $G(\mathbf{R}_s, \mathbf{R}_r)$ here is $\widehat{p}/\widehat{S}$ in Pierce's notation.)

Extending the free-space result to include contributions from the reflected paths, we have

$$\begin{aligned}\left\langle |p_i^\alpha|^2 \right\rangle = A^2 \Big[& |G(\mathbf{R}_{0,i} + \mathbf{R}_{b,i}, \mathbf{R}_{b,i})|^2 \delta V_i \sigma^\alpha(\theta_i) |G(\mathbf{R}_{b,i}, \mathbf{R}_i + \mathbf{R}_{b,i})|^2 \\ & + |G(\mathbf{R}_{w,i} + \mathbf{R}_{b,i}, \mathbf{R}_{b,i})|^2 \delta V_i \sigma^\alpha(\theta_i + \beta_i) |G(\mathbf{R}_{b,i}, \mathbf{R}_i + \mathbf{R}_{b,i})|^2 \\ & + |G(\mathbf{R}_{0,i} + \mathbf{R}_{b,i}, \mathbf{R}_{b,i})|^2 \delta V_i \sigma^\alpha(\theta_i + \chi_i) |G(\mathbf{R}_{b,i}, \mathbf{R}_{u,i} + \mathbf{R}_{b,i})|^2 \\ & + |G(\mathbf{R}_{w,i} + \mathbf{R}_{b,i}, \mathbf{R}_{b,i})|^2 \delta V_i \sigma^\alpha(\theta_i + \beta_i + \chi_i) |G(\mathbf{R}_{b,i}, \mathbf{R}_{u,i} + \mathbf{R}_{b,i})|^2 \Big] \end{aligned} \quad (45)$$

where $\mathbf{R}_{w,i}$ is the vector from the center of the scattering subvolume to the image source, $\mathbf{R}_{u,i}$ the corresponding vector to the image receiver, and the angles β_i and χ_i are defined in Fig. 5. The four terms in the equation correspond to the propagation paths SOR, WOR, SOU, and WOU, as described previously. The scattered contributions from each of the four paths are assumed to be uncorrelated in this formulation. The reader is referred to [21] for a discussion of path-correlation effects.

Except as otherwise noted, the calculations to follow in this section are based on a barrier of height 2.5 m, with $z_s = 0.5$ m, $x_s = -10$ m, $z_r = 1.2$ m, and $x_r = 15$ m. The total volume used for the scattering calculations spanned $-20\ \text{m} \leqslant x \leqslant 25$ m, $-20\ \text{m} \leqslant y \leqslant 20$ m, and $0\ \text{m} \leqslant z \leqslant 40$ m. This overall volume was partitioned into $60 \times 21 \times 60$ subvolumes. In the QW representation, the scale of the largest size class, a_1, is set to 5 m. This value, which is representative of the size of the largest shear-generated eddies in the vicinity of the barrier top, is also used for L_v. (In [16], it

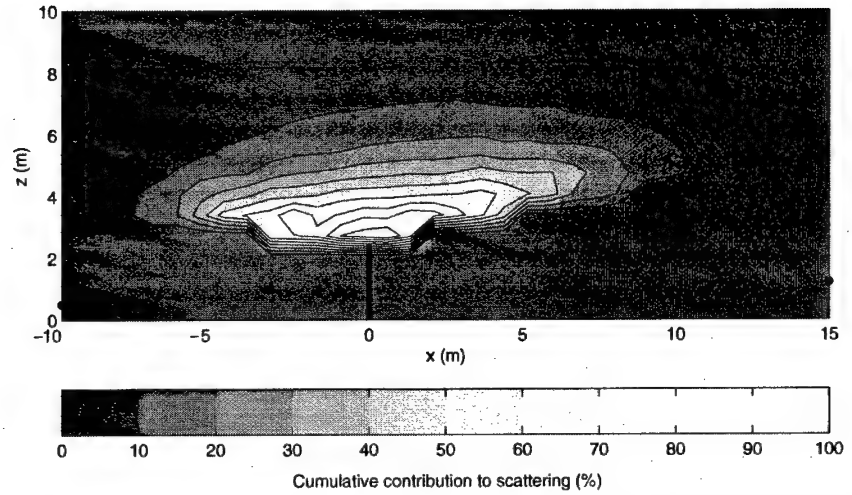

Fig. 6. Vertical cross-section through the region of primary scattering, as determined from the QW model. The calculation is for a frequency of 2000 Hz, barrier height 2.5 m, $z_s = 0.5$ m, $x_s = -10$ m, $z_r = 1.2$ m, and $x_r = 15$ m. Ten percent of the scattering occurs outside the 10% contour, 20% of the scattering occurs outside the 20% contour, etc.

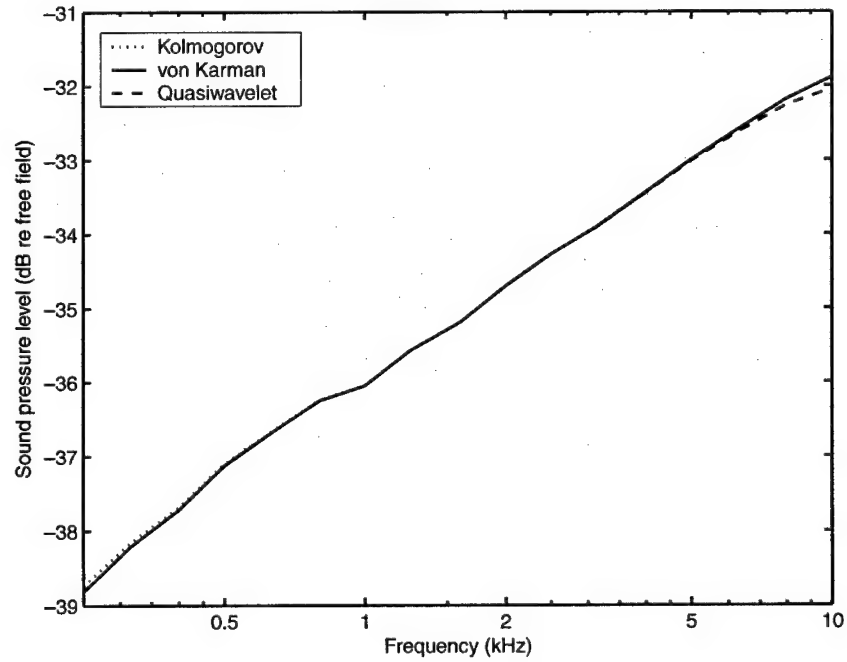

Fig. 7. Comparison of scattering calculations performed with the Kolmogorov, von Kármán, and QW models. A total of 128 QW size classes, ranging from $a_1 = 5$ m to $a_N = 0.005$ m, were used.

was shown that $L_v = 1.8z$ for shear-generated turbulence over flat ground, implying that $L_v = 5$ m when $z = 2.8$ m.) The scale of the smallest size class, a_N, is set to 0.005 m, which is characteristic of the Kolmogorov microscale in the atmosphere. A total of 128 size classes are used, in order to obtain a very smooth spectrum.

For simplicity, only turbulent velocity fluctuations generated by ground-based wind shear are explicitly included in the calculations; thermal turbulence and turbulence generated through interactions of the atmospheric flow with the barrier are neglected. This idealization is reasonable when the wind blows parallel to the barrier. For oblique wind angles, one can expect increased turbulence downwind of the barrier. The strength of the turbulent velocity fluctuations is specified with the friction velocity u_*, which is related to the dissipation rate through the equation $\epsilon = u_*^3/0.4z$, where z is set to 2.8 m [16]. (The turbulence parameters L_v and ϵ could have been made height dependent in generating the QW field, but this would complicate interpretation of the results.) Furthermore, only scattering elements with a line-of-sight to both the source and receiver are considered. Because the scattering model (based on von Kármán's spectrum) is valid in the forward directions, we need not restrict ourselves to scattering angles greater than 20°, as was necessary for earlier calculations [1] based on Kolmogorov's spectrum. The reason for considering only the line-of-sight paths is to make a clear physical distinction between the diffraction process and scattering by intrinsic atmospheric turbulence. Scattering along

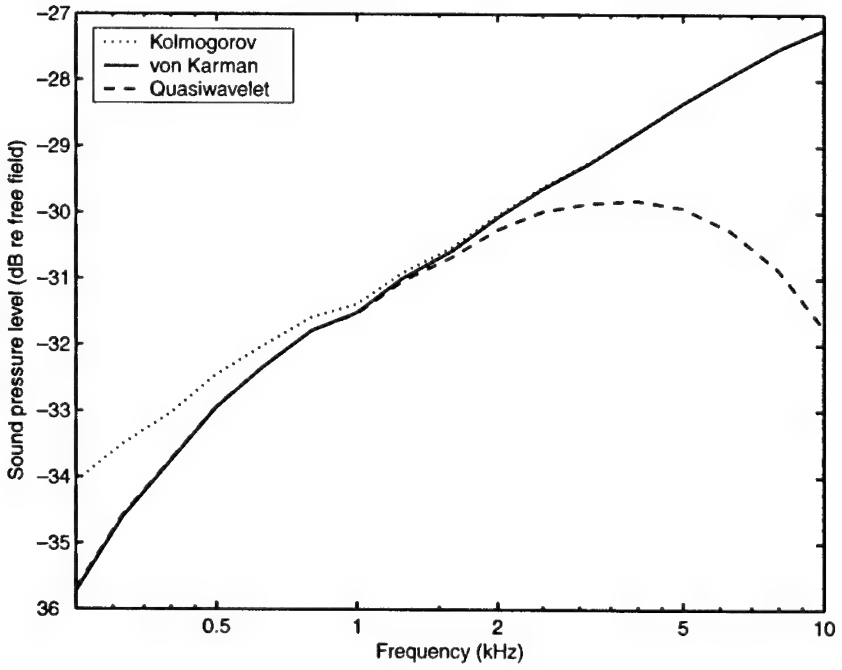

Fig. 8. Comparison of scattering calculations performed with the Kolmogorov, von Kármán, and QW models. A total of 128 QW size classes, ranging from $a_1 = 1$ m to $a_N = 0.025$ m, were used.

non-line-of-sight paths likely involves complicated interactions between the wind field and barrier, which have the additional effect of refracting sound. The reader is referred to [22,23] for discussions and models of these phenomena.

The calculated spatial extent of the scattering volume for this geometry at $f = 2000$ Hz is shown in Fig. 6. This figure was created by calculating the $\langle|p_i^\alpha|^2\rangle$ corresponding to each δV_i (using Eq. (43)), sorting the results in order of increasing $\langle|p_i^\alpha|^2\rangle$, and then cumulatively summing the resulting sequence. Note that the strongest scattering occurs in a small region immediately above the barrier. Scattering weakens substantially a few meters above the barrier or 5–10 m toward the source or receiver. Results for other frequencies (not shown) demonstrate that the appearance of the scattering volume does not change substantially over the frequency range considered in this paper.

Sound pressure levels (SPL) of the scattered fields corresponding to the von Kármán (Eq. (43)), Kolmogorov (large kL_v limit of Eq. (43)), and QW models are plotted in Fig. 7. The SPL is represented here as $10\log\langle|p_S|^2\rangle/|p_0|^2$, where p_0 is the pressure field in free space. For comparison purposes, a similar plot is presented in Fig. 8 except with the size of the largest QW class reduced fivefold and that of the smallest QW class increased fivefold ($a_1 = 1$ m and $a_N = 0.025$ m, with L_v in the von Kármán model changed accordingly). At low frequencies, the von Kármán and QW models give essentially the same result. This is to be expected, since they produce the

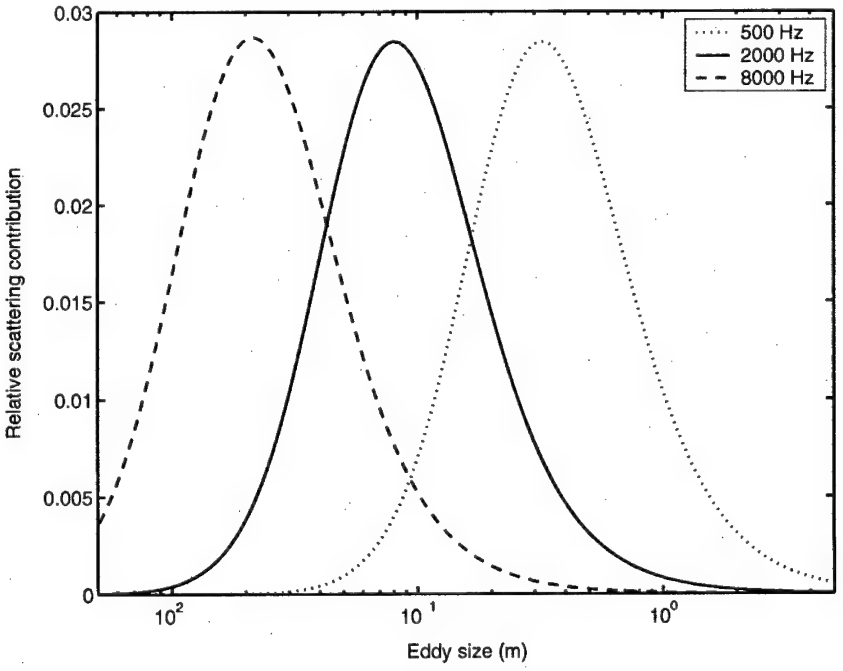

Fig. 9. Contribution to the scattered mean-square pressure as a function of eddy size, $\langle|p_S^\alpha|^2\rangle/\langle|p_S|^2\rangle$. Results for QW scattering at the frequencies 500, 2000, and 8000 Hz are shown.

same turbulence spectrum within the energy-containing and inertial subranges (Fig. 2). The Kolmogorov spectrum predicts a higher scattered SPL at low frequency, because it lacks a realistic spectral roll-off at low wavenumber. This effect is barely evident in Fig. 7 but is quite clear in Fig. 8, due to the smaller value of a_1. At higher frequency, the Kolmogorov and von Kármán models give the same results, whereas the QW model predicts a somewhat lower SPL. This is a result of the spectral roll-off in the dissipation subrange, which is included in the QW model but not the others. One may deduce from Fig. 7 that the Kolmogorov spectrum is a reasonable approximation for the scenario, even at frequencies as low as 250 Hz. This outcome is very dependent upon the barrier geometry and outer length scale of the turbulence, however.

Fig. 9 shows the scale of the eddies (QWs) responsible for the scattering for the frequencies 500, 2000, and 8000 Hz. Specifically, the ratio $\langle|p_S^\alpha|^2\rangle/\langle|p_S|^2\rangle$ at the receiver position is plotted. The maxima for these curves appear at $a_\alpha \simeq 0.30$ m for 500 Hz, $a_\alpha \simeq 0.080$ m for 2000 Hz, and $a_\alpha \simeq 0.022$ m for 8000 Hz. As shown in Section 3, the scattering cross-section is maximized for the size class α such that $a_a/a_1 = \sqrt{17/6}/[2kL_v \sin(\theta/2)]$. Taking 3 m as the nominal height of the scattering volume, and assuming that the horizontal center of the scattering volume is above the barrier, implies a scattering angle of about 20° for the unreflected path SOR. With $a_1 = L_v$, we therefore have $a_\alpha \simeq 260f^{-1}$ m for SOR. Maximum scattering is

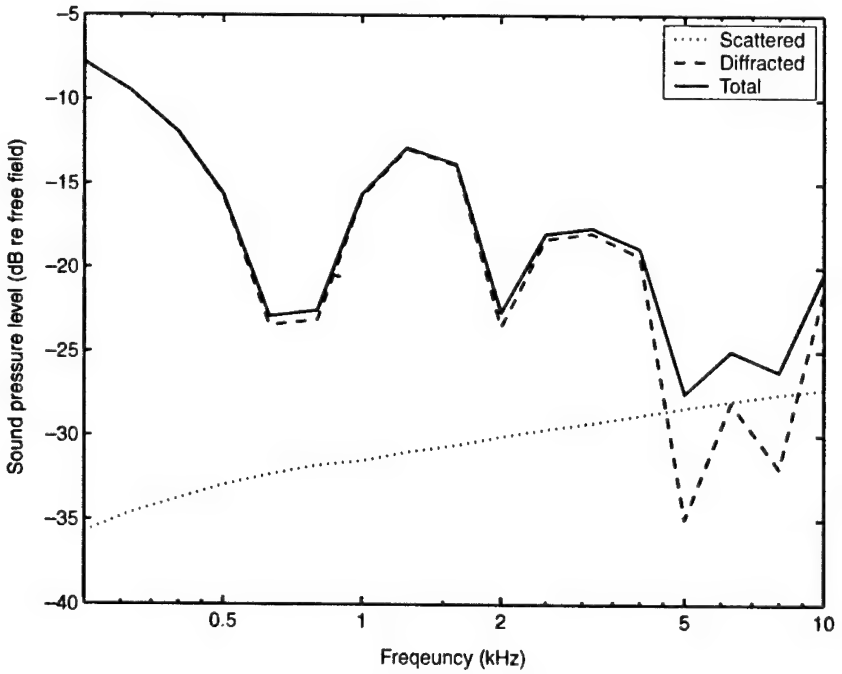

Fig. 10. Scattered, diffracted, and total SPL as a function of frequency. The barrier height is 2.5 m and the friction velocity (a measure of the strength of the turbulence) is 0.6 m s^{-1}.

thus expected to occur at $a_\alpha \simeq 0.52$ m for 500 Hz, $a_\alpha \simeq 0.13$ m for 2000 Hz, and $a_\alpha \simeq 0.032$ m for 8000 Hz. These values are 45–70% larger than the locations of the calculated peaks. However, it must be kept in mind that the the actual scattering volume is distributed in space, and that the regions distant from the barrier are characterized by higher scattering angles. Furthermore, the ground-reflected paths have higher scattering angles. A repeat of this exercise for the double reflection path, WOR, yields a scattering angle of about 35°, $a_\alpha \simeq 150 f^{-1}$ m, $a_\alpha \simeq 0.30$ m for 500 Hz, $a_\alpha \simeq 0.075$ m for 2000 Hz, and $a_\alpha \simeq 0.019$ m for 8000 Hz. These values are much closer to the theoretical result, thereby suggesting the correctness of the theory. It is also interesting that the scattering contributions have a distinctly normal (bell-curve) appearance when plotted as a function of the logarithm of the eddy size. Most of the scattering occurs from eddy sizes between one-half and twice the peak scattering size.

The frequency dependence of the scattered, diffracted, and total received SPL is shown in Fig. 10. The diffracted field was calculated with Pierce's formula [20, Eq. (9-9.1)]. The scattered field in this example was calculated from the friction velocity $u_* = 0.6$ m s^{-1}, which corresponds to $C_v^2 = 0.47$ m$^{4/3}$s^{-2} at 2.8 m height and is a rather large value for the atmosphere [24]. (In practice, the barrier may generate additional turbulence, effectively raising u_*.) Only for frequencies above approximately 4 kHz does scattering significantly affect the observed SPL. This outcome is in

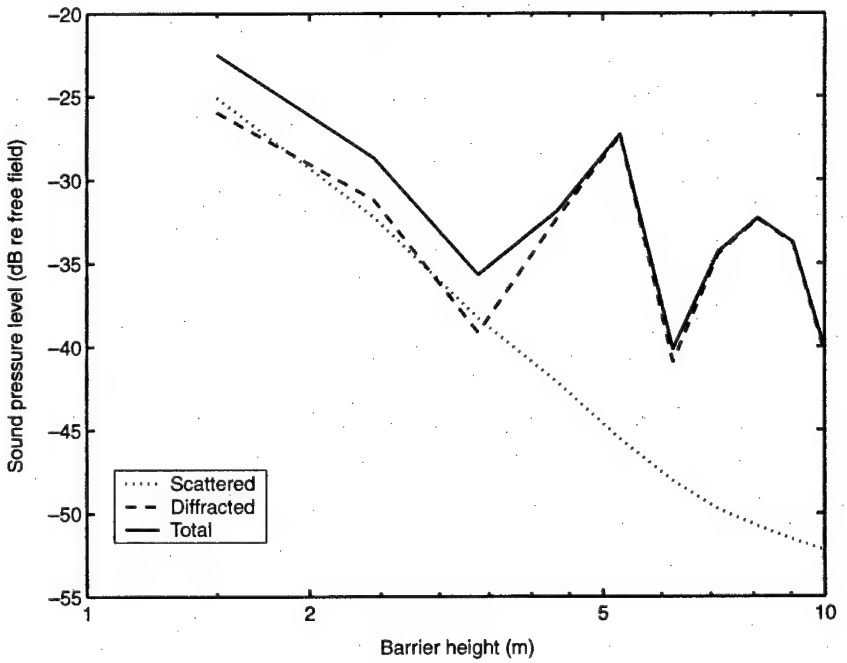

Fig. 11. Scattered, diffracted, and total SPL as a function of barrier height. The heights and horizontal distances of the source and receiver are held constant. The calculation is for $f = 8000$ Hz and a friction velocity of 0.6 m s^{-1}.

broad agreement with Fig. 8 from [1], although the details of the frequency dependence are different here due to the inclusion of the ground-reflection paths.

Fig. 11 shows the received SPL at 8000 Hz as a function of the barrier height. The heights of the source and receiver, and their horizontal distances from the barrier, were held fixed to the values given earlier. For barrier heights less than about 4 m, the scattered contribution is roughly equal to the diffracted one. At greater heights, and therefore at larger scattering angles, the diffracted contribution is more prominent. Fig. 12 is similar to Fig. 11, except that the received SPL at 8000 Hz is shown as a function of the horizontal separation between the barrier and receiver (x_r). The barrier height for Fig. 12 is again 2.5 m and the horizontal distance to the source remains fixed at $x_s = -10$ m. As the distance of the receiver from the barrier increases, the scattering angle becomes smaller and therefore the scattered energy becomes more significant. Also note that as the distance increases the effects of multiple scattering in the direction of sound propagation become more important. These effects, however, result mainly in fluctuations in the phase and amplitude of a sound wave reaching the receiver while the intensity of the wave remains approximately unchanged.

Last, Fig. 13 shows the scattered, diffracted, and total received SPL at 8000 Hz as a function of the friction velocity. As u_* increases past 0.6 m s^{-1}, the scattered

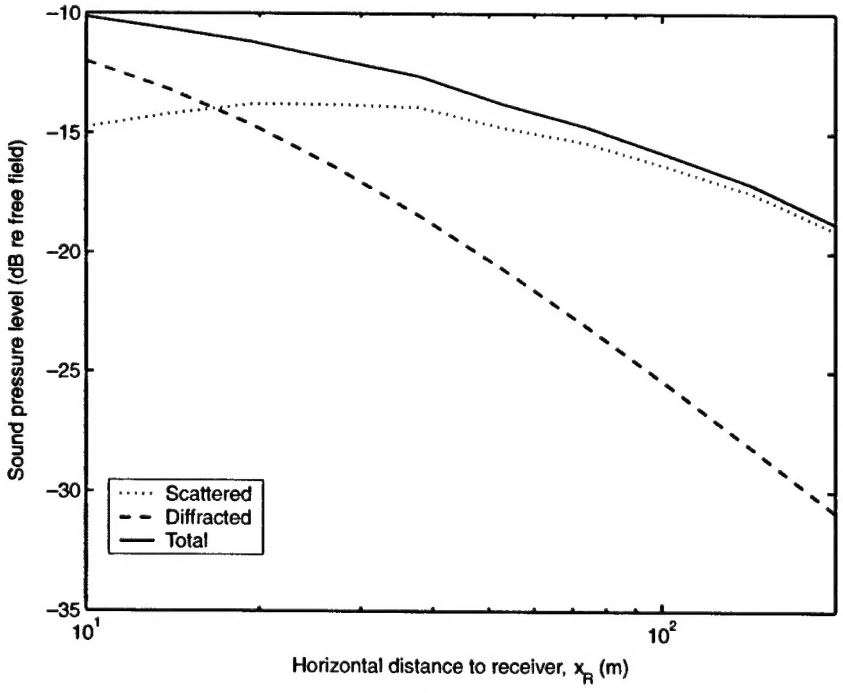

Fig. 12. Scattered, diffracted, and total SPL as a function of horizontal distance between the barrier and receiver. The heights of the source and receiver, and the horizontal distance to the source, are held constant. The calculation is for $f = 8000$ Hz, a barrier height of 2.5 m and a friction velocity of 0.6 m s^{-1}.

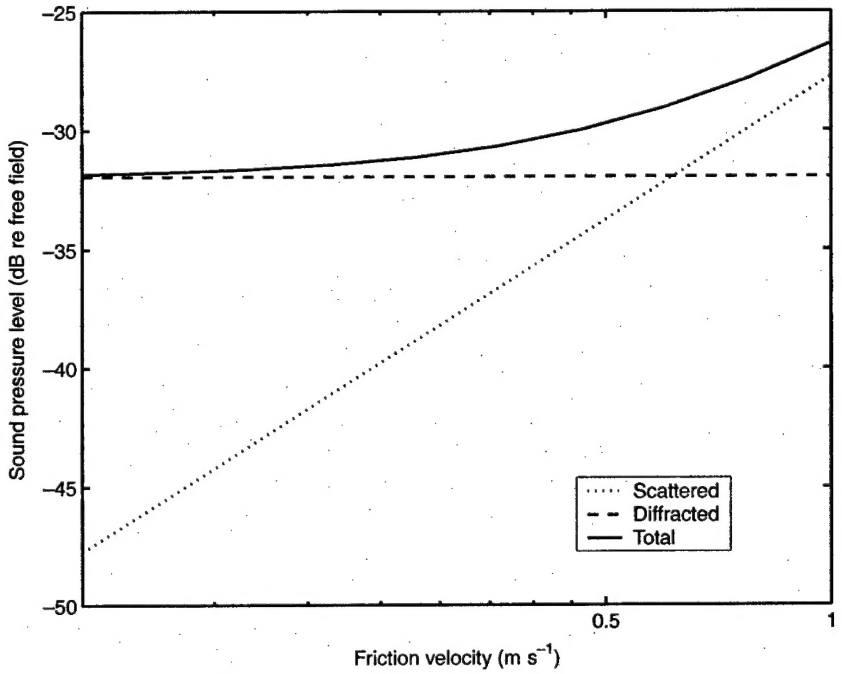

Fig. 13. Scattered, diffracted, and total SPL as a function of the friction velocity of the turbulence. Results for the friction velocity varying from 0.1 to 1 m s^{-1} are shown. The calculation is for $f = 8000$ Hz and a barrier height of 2.5 m.

contribution overtakes the diffracted one. Taken together, Figs. 10–13 demonstrate that turbulent scattering is significant primarily at high frequencies and for relatively short barriers. This outcome is consistent with Fig. 4, which shows that the scattering cross-section is highest for nearly forward scattering at large values of kL_v. Strong turbulence, either already intrinsic to the atmosphere or injected by flow disturbances from the barrier or other nearby objects, must be present for significant scattering.

5. Conclusion

As was first demonstrated by Daigle [1], turbulence diminishes the effectiveness of noise barriers by scattering sound energy over them. Daigle's calculation of the scattered sound energy was based on the scattering cross-section for inertial subrange turbulence, namely the large kL_v limit of Eq. (44). In this paper, we have performed scattering calculations similar to Daigle's, although the recently introduced quasi-wavelet (QW) representation was used. The QW representation mimics the conceptual picture of turbulence consisting of a number of discrete, randomly placed eddies whose sizes span a range of spatial scales. Parameters of the QW

representation, such as the number of eddies, their size distribution, and angular velocities, can be chosen to reproduce known models for the atmospheric turbulence spectrum. When applied to scattering, the QW representation provides a concise decomposition of the scattering as a function of the eddy size and location. Also, since the QW parent function was derived in this paper on the basis of von Kármán's spectrum, it can be applied to scattering from the energy-containing subrange and therefore to small scattering angles.

An expression for the scattering cross-section of an ensemble of randomly oriented QWs of a particular size was derived in this paper. When the scattered energies of all of the QW size classes were added together, and the continuous size limit taken, the total scattering cross-section agreed with a previously derived result for the von Kármán turbulence spectrum. An expression for the eddy size that maximizes scattering, as a function of the acoustic wavenumber and scattering angle, was also derived. Calculations showed that, for a typical barrier condition, most of the scattered energy originates from eddies in the size range of approximately one-half to twice the size of the eddies responsible for maximum scattering.

The results in this paper suggest that scattering behind the barrier attributable to "line-of-sight" eddies, namely those with a line of sight to both the source and receiver, is generally significant only for frequencies above several kilohertz, for sources and receivers no more than a few meters below the top of the barrier, and for very turbulent atmospheric conditions.

Acknowledgements

D.K. Wilson's contribution to this paper was supported by the US Army Engineer Research and Development Center AT24 work package. The contributions of V.E. Ostashev and G.H. Goedecke were supported by US Army Research Office Grant DAAG19-01-1-0640.

References

[1] Daigle GA. Diffraction of sound by a noise barrier in the presence of atmospheric turbulence. J Acoust Soc Am 1982;71:847–54.
[2] Goedecke G, Auvermann HJ. Acoustic scattering by atmospheric turbules. J Acoust Soc Am 1997;102:759–71.
[3] Goedecke G, Ostashev VE, Wilson DK, Auvermann HJ. Quasi-wavelet model of von Kármán and other velocity spectra. Boundary-Layer Meteorol [in press].
[4] Goedecke GH, Wood RC, Auvermann HJ, Ostashev VE, Havelock DI, Ting C. Spectral broadening of sound scattered by advecting atmospheric turbulence. J Acoust Soc Am 2001;109:1923–34.
[5] deWolfe D. A random motion model of fluctuations in a nearly transparent medium. Radio Sci 1983;83:138–42.
[6] McBride WE, Bass HE, Raspet R, Gilbert KE. Scattering of sound by atmospheric turbulence: a numerical simulation above a complex impedance boundary. J Acoust Soc Am 1991;90:3314–25.
[7] Boulanger P, Raspet R, Bass HE. Sonic boom propagation through a realistic turbulent atmosphere. J Acoust Soc Am 1995;98:3412–7.

[8] Hinze JO. Turbulence. New York: McGraw-Hill; 1975.
[9] Batchelor GK. The theory of homogeneous turbulence. Cambridge, UK: Cambridge University Press; 1953.
[10] Farge M. Wavelet transforms and their applications to turbulence. Ann Rev Fluid Mech 1992;24:395–457.
[11] Meneveau C. Analysis of turbulence in the orthonormal wavelet representation. J Fluid Mech 1994;232:4469–520.
[12] Kolmogorov AN. The local structure of turbulence in incompressible viscous fluid for very large Reynolds numbers, Dokl Akad Nauk SSSR 1941;30:299–303 [English Transl.: Proc R Soc London, Ser A 1991;434:9–13].
[13] Kaimal JC, Wyngaard JC, Izumi Y, Coté OR. Spectral characteristics of surface layer turbulence. Quart J Roy Meteorol Soc 1972;98:563–89.
[14] Högström U. Review of some basic characteristics of the atmospheric surface layer. Boundary-Layer Meteorol 1996;78:215–46.
[15] Ostashev VE, Brähler B, Mellert V, Goedecke GH. Coherence functions of plane and spherical waves in a turbulent medium with the von Karman spectrum of medium inhomogeneities. J Acoust Soc Am 1998;104:727–37.
[16] Wilson DK. A turbulence spectral model for sound propagation in the atmosphere that incorporates shear and buoyancy forcings. J Acoust Soc Am 2000;108:2021–38.
[17] Gradshteyn IS, Ryzhik IM. Table of integrals, series and products. San Diego: Academic Press; 1994.
[18] Ostashev VE. Acoustics in moving inhomogeneous media. London: E&FN Spon; 1997.
[19] Ostashev VE, Goedecke GH. Sound scattering cross section for von Karman spectra of temperature and wind velocity fluctuations. In: Richter JH, Anderson KD, editors. Proceedings of the 1997 Battlespace Atmospherics Conference. San Diego, CA: NCCOSC; 1998. p. 171–80.
[20] Pierce AD. Acoustics: an introduction to its physical principles and applications. Woodbury, NY: Acoustical Society of America; 1989.
[21] Forssén J, Ögren M. Thick barrier noise-reduction in the presence of atmospheric turbulence: measurements and numerical modelling. Appl Acoust 2002;63:173–87.
[22] Salomons EM. Reduction of the performance of a noise screen due to screen-induced wind-speed gradients. numerical computations and wind-tunnel experiments. J Acoust Soc Am 1999;105:2287–93.
[23] Blumrich R, Heimann D. A linearized Eulerian sound propagation model for studies of complex meteorological effects. J Acoust Soc Am 2002;112:446–55.
[24] Stull RB. An introduction to boundary layer meteorology. Dordrecht, Germany: Kluwer; 1988.